Nanoscale

ROYAL SOCIETY OF CHEMISTRY

PAPER

View Article Online
View Journal | View Issue

Cite this: *Nanoscale*, 2022, **14**, 3441

Fast and recoverable NO_2 detection achieved by assembling ZnO on $Ti_3C_2T_x$ MXene nanosheets under UV illumination at room temperature†

Chao Fan, Jia Shi, Yongwei Zhang, Wenjing Quan, Xiyu Chen, Jianhua Yang, * Min Zeng, Zhihua Zhou, Yanjie Su, Hao Wei and Zhi Yang *

Recently, $Ti_3C_2T_x$ MXenes have begun to receive attention in the field of gas sensors owing to their characteristics of high conductivity and abundant surface functional groups. However, $Ti_3C_2T_x$-based gas sensors still suffer from the drawbacks of low sensitivity and sluggish response/recovery speed towards target gases, limiting their development in further applications. In this work, $Ti_3C_2T_x$–ZnO nanosheet hybrids were fabricated through a simple sonication method. The $Ti_3C_2T_x$–ZnO nanosheet hybrids exhibited a short recovery time (10 s) under UV (ultraviolet) illumination, a short response time (22 s), a high sensitivity (367.63% to 20 ppm NO_2) and selectivity. Furthermore, the $Ti_3C_2T_x$–ZnO sensor has prominent anti-humidity properties, as well as superior reproducibility in multiple tests. The abundant active sites in the $Ti_3C_2T_x$–ZnO nanosheet hybrids, including surface groups (–F, –OH, –O) of $Ti_3C_2T_x$ and oxygen vacancies of ZnO, the formation of Schottky barriers between $Ti_3C_2T_x$ and ZnO nanosheets and the rich photogenerated charge carriers of ZnO under UV illumination, together result in excellent gas-sensing performance. Density functional theory calculations have been further employed to explore the sensing performance of $Ti_3C_2T_x$ and ZnO nanosheets, showing strong interactions existing between the NO_2 and ZnO nanosheets. The main adsorption sites for NO_2 were present on the ZnO nanosheets, while the $Ti_3C_2T_x$ played the role of the conductive path to accelerate the transformation of charge carriers. Our work can provide an effective way for improving the gas-sensing performances of $Ti_3C_2T_x$-based gas sensors.

Received 15th October 2021,
Accepted 21st January 2022

DOI: 10.1039/d1nr06838e

rsc.li/nanoscale

Introduction

With the acceleration of industrial production and the continued increasing use of automobiles, a large quantity of toxic and harmful gases, such as NO_2, SO_2 and NO, *etc.*, is discharged into the atmosphere.[1,2] Among these harmful gases, NO_2 is a toxic gas that mainly damages the respiratory tract of humans.[3,4] When people are exposed to an environment containing NO_2 gas for serval minutes, they will have symptoms of chest tightness, respiratory distress and cough.[5,6] The reported upper exposure limit of NO_2 gas concentration for humans is 20 ppm.[7] The respiratory tract and nervous system become seriously injured following exposure to NO_2 environments above this concentration over long periods of time.[8] In addition, the discharge of large amounts of NO_2 can lead to the phenomenon of acid rain, which pollutes soil and water environments. Therefore, fast detection of NO_2 gas and timely feedback are extremely important for the health of people and of the environment.[9–11]

In recent years, two-dimensional layered material such as graphene,[12–15] transition metal dichalcogenide-based materials,[16–19] black phosphorus,[20–22] MXene,[23,24] *etc.*, have attracted much attention owing to their great promise as gas sensors at room temperature.[25–27] Among these materials, MXene has become a promising candidate for gas-sensitive material that can operate at room temperature because of its low signal-to-noise ratio, rich surface functional groups (–OH, –F, –O) and high electron conductivity.[28–30] $Ti_3C_2T_x$ is one of the earliest discovered MXene materials, which exhibits metallic conductivity, and it has been widely studied in recent years. However, it has remained a major challenge to improve the poor sensitivity and response/recovery speed of $Ti_3C_2T_x$ MXene-based sensors.

Resistance modulation of Schottky barriers can effectively improve current transport efficiency and induce a high NO_2

Key Laboratory of Thin Film and Microfabrication (Ministry of Education), Department of Micro/Nano Electronics, School of Electronic Information and Electrical Engineering, Shanghai Jiao Tong University, Shanghai 200240, P. R. China. E-mail: yangjh08@sjtu.edu.cn, zhiyang@sjtu.edu.cn

†Electronic supplementary information (ESI) available. See DOI: 10.1039/d1nr06838e

sensing response.[31] In addition, the construction of MXene/metal oxide semiconductor composites has been considered to be an effective method to improve the NO_2 sensing properties of $Ti_3C_2T_x$ MXene-based gas sensors. Since the $Ti_3C_2T_x$ MXene material displays a layer-like structure, metal oxide semiconductors can easily interact with $Ti_3C_2T_x$. For example, Choi *et al.* developed TiO_2/Ti_3C_2 MXene materials through the *in situ* oxidation method and tailored the oxidation time to change the number of Schottky barriers. The TiO_2/Ti_3C_2 sensor exhibited higher NO_2 sensitivity compared with the bare Ti_3C_2 MXene material.[32] Sun *et al.* reported Co_3O_4 nanoparticle-based polyethyleneimine-functionalized $Ti_3C_2T_x$ MXene sheets, which showed a high gas response and fast response time (below 2 s) towards NO_2 gas at room temperature.[33] Chen *et al.* reported that the nanohybrid of SnS_2 and MXene-derived TiO_2 exhibited a large response and ultra-fast recovery towards NO_2 gas.[34]

ZnO, a typical n-type metal–oxide–semiconductor material, with a wide bandgap of 3.37 eV, excellent chemical stability and rich oxygen vacancies has emerged as a promising gas-sensitive material.[35–38] In particular, ZnO or ZnO composite materials have been widely applied as NO_2 sensors at room temperature in recent years.[39] This is because of the abundant defects and the feasibility of shape control of ZnO.[40,41] For example, Moon *et al.* reported that nanohybrid materials of reduced graphene oxide and ZnO nanorods exhibited ultra-high sensitive detection to 40 ppb of NO_2 and a short response/recovery time.[42] Hung *et al.* prepared biaxial p-SnO/n-ZnO nanowire heterostructures with enhanced performance for detection of ppb-level NO_2 at room temperature.[43] Song *et al.* produced ZnO nanoflowers by a hydrothermal method, and the fabricated sensor displayed an improved NO_2 sensing property (response of 128 to 1 ppm NO_2) and a low detection limit (50 ppb).[44] To facilitate the recovery speed of the gas sensors, UV illumination has been widely applied and recognized as an effective way to enhance the properties of the recovery characteristics of gas sensors.[45,46] The main reason for this is that photogenerated barriers can clean the surface of materials, which can accelerate the desorption process.[47] Zheng *et al.* reported that the InSe nanosheet sensor can achieve rapid and full recovery to NO_2 gas within 169 s under UV illumination.[48] Zhou *et al.* presented the Au-MoS_2 gas sensor, which achieved better sensing properties, including three times the response and full recovery under illumination compared with that in the dark.[49] Wu *et al.* found that the recovery rate of the p-type $MoTe_2$ gas sensor to different concentrations of NO_2 was significantly improved under UV illumination.[50] In addition, many studies have shown that ZnO exhibits outstanding NO_2 sensing performances under UV illumination because of its excellent optoelectronic properties.[51–53] As a result, construction of the $Ti_3C_2T_x$–ZnO Schottky junction with the assistance of UV illumination can combine the excellent properties of these two materials, which is expected to result in further enhancement of the NO_2 sensing properties.

To the best of our knowledge, most $Ti_3C_2T_x$ MXene-based NO_2 sensors are still unable to achieve the properties of fast response and recovery speed at the same time. Few researchers have reported $Ti_3C_2T_x$–ZnO nanosheet hybrid NO_2 sensors.[54,55] Herein, we propose $Ti_3C_2T_x$–ZnO nanosheet hybrids with Schottky barriers for NO_2 sensing and recovery under UV illumination. The $Ti_3C_2T_x$ nanosheets were synthesized using the conventional method of HF solution etching of the Al layer of Ti_3AlC_2 (MAX). ZnO nanosheets were prepared by hydrothermal and calcination methods, with Zn $(CH_3COOH)_2{\cdot}2H_2O$, urea and polyvinylpyrrolidone (PVP) as the precursors. The porous morphology for the ZnO nanosheets was successfully obtained, which is helpful for the adsorption of NO_2 gas. With the assistance of UV irradiation in the recovery process, the $Ti_3C_2T_x$–ZnO nanosheet-based gas sensor exhibited better NO_2 sensing properties, including high sensitivity (367.63% to 20 ppm NO_2), shorter response/recovery time (22 s/10 s), excellent repeatability and superior humidity resistance properties, in comparison to pristine $Ti_3C_2T_x$ and ZnO materials. Density functional theory (DFT) calculations indicated that the main adsorption sites were on the surface of the ZnO nanosheets, with $Ti_3C_2T_x$ mainly playing the role of the conductive pathway, which can accelerate the transfer efficiency of carriers between $Ti_3C_2T_x$ and ZnO materials.

Jianhua Yang

Dr Jianhua Yang is an Assistant Professor at the Department of Micro/Nano Electronics, Shanghai Jiao Tong University. His degrees are in materials science with a BSc in 2012 from Lanzhou University, an MSc in 2015 with Professor Ying Yu at Central China Normal University, and a PhD in 2018 with Professor Jianfang Wang at The Chinese University of Hong Kong (CUHK). He worked as a postdoctoral researcher at CUHK from 2018 to 2020. His research interests involve the rational design and synthesis of nanomaterials for gas sensors at room temperature, the fabrication of flexible pressure sensors, and plasmonic photocatalysis.

Experimental

Synthesis of $Ti_3C_2T_x$ MXene

$Ti_3C_2T_x$ MXene nanosheets were fabricated using the previously reported methods.[56] Typically, 0.5 g of Ti_3AlC_2 powder was dispersed in 20 mL HF solution and stirred for 24 h at room temperature. The solution after etching was washed with deionized (DI) water and centrifuged at 8500, 5500 and 3500 rpm, for 5 min each, until the pH of the supernatant reached 6.0. Subsequently, the obtained material was dried at 60 °C overnight in a vacuum drying oven.

Synthesis of ZnO nanosheets

ZnO nanosheets were synthesized through a simple hydrothermal and calcination approach. Typically, 1.1 g of Zn $(CH_3COOH)_2{\cdot}2H_2O$ was dissolved in 40 mL DI water by vigorous stirring for 10 min. Then, 0.6 g urea and 0.2 g PVP (M_w = 58 000) were added into the solution with stirring for 20 min. Afterwards, the solution was transferred into a 50 mL Teflon-lined autoclave, which was then heated at 120 °C in a furnace for 6 h. Finally, the solution was washed with DI water and ethanol and centrifuged at 8000 rpm for 10 min. After drying in the vacuum furnace at 60 °C for 12 h, the collected powder was calcinated at 450 °C for 2 h with a heating rate of 5 °C min^{-1}.

Synthesis of $Ti_3C_2T_x$–ZnO nanosheet hybrids

The $Ti_3C_2T_x$–ZnO nanosheet hybrids were prepared *via* a facile sonication method. First, 25 mg of $Ti_3C_2T_x$ was dispersed in 50 mL DI water and sonicated for 30 min. After that, 10 mg of ZnO nanosheets were added into the above dispersion, followed by sonication for another 30 min at a power of 100 W. Finally, the dispersion was centrifuged six times at 8500 rpm for 5 min with DI water. After drying in a vacuum furnace at 60 °C for 12 h, the $Ti_3C_2T_x$–ZnO nanosheet hybrids were collected. The samples of ZnO nanosheets and $Ti_3C_2T_x$–ZnO nanosheet hybrids were labeled as ZnO NS and $Ti_3C_2T_x$–ZnO NS, respectively.

Material characterizations

The morphologies of $Ti_3C_2T_x$ MXene nanosheets, ZnO NS and $Ti_3C_2T_x$–ZnO NS were observed by scanning electron microscopy (SEM, Ultra Plus, Carl Zeiss, Germany), transmission electron microscope (TEM, JEM-2100, JEOL, Japan) and scanning transmission electron microscopy (STEM, JEM-2100, JEOL, Japan). The elemental analysis of $Ti_3C_2T_x$–ZnO NS was obtained by energy-dispersive X-ray spectroscopy (EDX) attached to TEM (JEM-2100, JEOL, Japan). The X-ray diffraction (XRD) patterns of samples were analyzed by an X-ray diffractometer (Bruker, Germany) with CuKα radiation (λ = 0.154056 nm) and the 2θ range was 0° to 80° with a scan speed of 5° min^{-1}. The element composition and internal bonding were collected by X-ray photoelectron spectroscopy (XPS, Japan Kratos Axis Ultra DLD, AlKα, 1486.6 eV). Raman spectral results were obtained using a Raman spectrometer with a 532 nm laser as the excitation source (inVia Reflex, RENISHAW, England). The specific surface areas were analyzed by the Brunauer–Emmett–Teller (BET) method based on the nitrogen adsorption–desorption isothermals at 77 K (Micromeritics ASAP 2460, USA).

Gas sensor fabrication and sensing measurements

The gas sensor was composed of interdigital electrodes and a thin layer of gas-sensing material. The interdigital electrode consisted of a 180 nm Au layer and 20 nm Ti layer on the Si/SiO_2 substrate, as shown in Fig. S1.† In the fabrication process of the layer of gas-sensing material, $Ti_3C_2T_x$–ZnO NS were first dispersed in DI water and sonicated for 10 min. Then, 5 μL DI water dispersion-contained materials were dropped onto the electrodes and dried at 60 °C for 2 h in the furnace. SEM images of the bare interdigital electrode and of the electrode covered with gas-sensing materials are shown in Fig. S2a and b.† For the sensing measurements, the gas sensor was put into a chamber and the gas-sensing performance was tested through the gas-sensing system. The signal was obtained using an Agilent 4156 C, which maintained a voltage of 0.5 V during the testing process. The flow rate of the gas was adjusted by the mass flow controllers (MFCs). The concentration of gas was changed using the mixer, which can mix the target gas with carrier air. For selectivity tests of the gas sensor, the standard NO_2 gas cylinder was replaced by a corresponding standard gas cylinder, including CO_2, H_2, NH_3 and hexanal. The effect of humidity on the gas sensor was tested on a simple home-made gas-line system as shown in Fig. S3† ranging from 0% to 80% relative humidity (RH). The response of the gas sensor is defined as $R_s = |R_g - R_a|/R_a \times 100\%$, where R_a is the resistance value of the gas sensor after stabilization in air and R_g is the resistance value of the gas sensor after exposure in NO_2 for a time. In the experiments, the wavelength of UV light-emitting diode (LED) light adopted was 365 nm. The distance between the gas sensor and UV LED light was 4 cm and the power of the UV LED light was 0.15 W. The selected light intensity was fixed at 3 mW cm^{-2}.

DFT calculations

The interactions between electrons and ions were examined using the projector augmented wave pseudopotentials.[57] The geometry relaxation, electronic calculations and the self-consistent field calculations of the $Ti_3C_2T_x$ and ZnO nanosheets were completed using DFT and operated in the Vienna *ab initio* simulation package.[58,59] The DFT-D3 correction method was considered to describe the van der Waals interactions between the gas molecules and the substrate.[60] The Perdew–Burke–Ernzerhof function within the generalized gradient approximation analysis was conducted to assess the exchange–correlation function.[61] A plane-wave basis set with a cut-off energy of 450 eV was used to expand the one-electron wave function.[62] The periodic structure of a 3 × 3 × 1 supercell of $Ti_3C_2T_x$ and ZnO with a vacuum thickness of 15 Å was used to simulate the interface of $Ti_3C_2T_x$ and ZnO. A 3 × 3 × 1 *k*-grid mesh sampling was used for geometry optimization, which was used for calculating the electronic structure to obtain a more precise result. All the calculations were carried out until the energy and the Hellmann–Feynman force reached the convergence criteria of 10^{-6} and 0.01 eV $Å^{-1}$, respectively. The Bader charge analysis developed by Henkelman was used to analyze the charge transfer between the gas molecule and the substrate materials.[63]

Results and discussion

The schematic diagram displayed in Fig. 1 illustrates the etching and subsequent sonication process for preparing

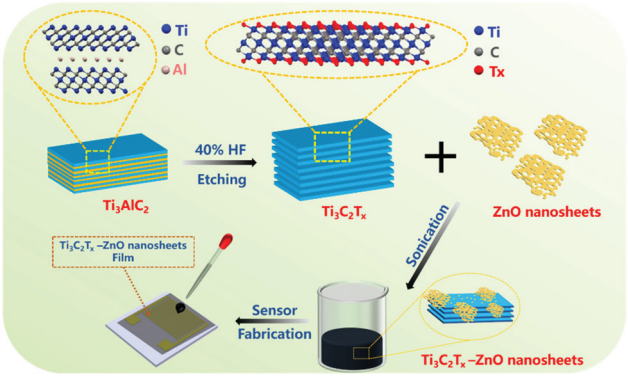

Fig. 1 Schematic diagram of the fabrication process of $Ti_3C_2T_x$–ZnO nanosheet hybrids and the gas sensor.

$Ti_3C_2T_x$–ZnO NS and the corresponding gas sensor. Briefly, the $Ti_3C_2T_x$ was produced by etching the Ti_3AlC_2 (MAX) in a 20 mL HF solution at room temperature. Hydrothermal and calcination methods were employed to synthesize the ZnO nanosheets. Finally, the obtained $Ti_3C_2T_x$ nanosheets were hybridized with ZnO NS by sonication treatment. The materials were dispersed in DI water and dropped onto the interdigital electrode to fabricate the gas sensor.

Fig. 2 shows the schematic diagram of the system for the sensing performance tests. The compressed air cylinder was used to provide the carrier gas, which was mixed with the target gas to produce different concentrations of target gas. The main function of the gas mixer was to deliver even levels of target gas with a certain concentration. MFCs were used to control the flow rate of compressed air and NO_2 gas. Gas sensors were fixed in a microchamber and connected with the Agilent 4156 C and computer using electric wires. After gas sensor exposure to NO_2 gas, UV LED light with 3 mW cm^{-2} light intensity was used to assist in recovery of the gas sensor to the original state. The humidity gas-sensing properties of the sensors were tested through the system shown in Fig. S3.†

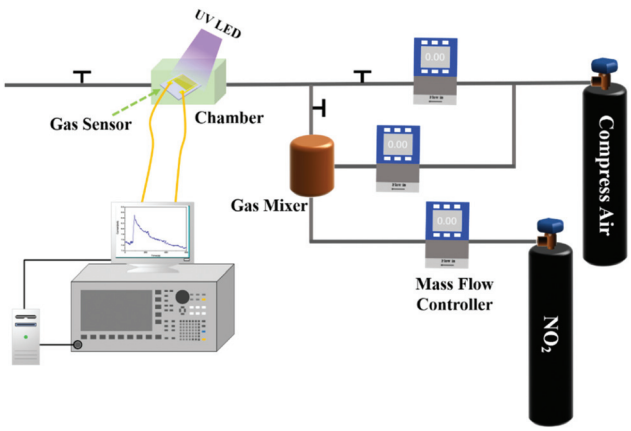

Fig. 2 Schematic diagram of the system for gas-sensing performance tests.

Compressed air passed through a flask filled with purified water to produce air with humidity, which was then passed through the chamber where the sensor was located. The humidity conditions were adjusted by changing the flow rate of compressed air *via* MFCs. The photoelectronic characteristics of $Ti_3C_2T_x$–ZnO nanosheet hybrids were examined by *I*–*V* curves (Fig. S4†). In the dark, the $Ti_3C_2T_x$–ZnO NS exhibited a linear curve that estimated the ohmic contact between $Ti_3C_2T_x$–ZnO NS and electrodes.[32] The $Ti_3C_2T_x$–ZnO NS under UV illumination displayed a nonlinear curve, which is mainly because the production of photogenerated carriers breaks the balance of the built-in electric field at the interface of $Ti_3C_2T_x$ and ZnO. The photogenerated electrons on the conduction band of ZnO will transfer to the $Ti_3C_2T_x$ until formation of a new balance.[46] It can be seen that after illumination with UV light, the current varies from 0.99 nA to 9.32 nA. The change in current is caused by the increase in the concentration of photogenerated electrons transferred from ZnO to the $Ti_3C_2T_x$.

The XRD patterns of Ti_3AlC_2, $Ti_3C_2T_x$ and $Ti_3C_2T_x$–ZnO NS are shown in Fig. 3. The characteristic peaks corresponding to the (002) plane shifted from 9.5° to 8.9° and the intensity of the peak has weakened at the same time. The (104) peak at 38.7° of Ti_3AlC_2 disappeared, indicating that the Al layer has been fully etched. Meanwhile, some new characteristic peaks appeared, such as for (004), (006) and (110), illustrating the successful fabrication of $Ti_3C_2T_x$. The XRD pattern shown in Fig. S5† reveals the high crystallinity, and no impurities exist in the ZnO NS. The peaks at 31.8°, 34.3°, 36.2°, 47.5°, 56.6° and 62.8° correspond to (100), (002), (101), (102), (110) and (103) planes, respectively. In the XRD pattern of $Ti_3C_2T_x$–ZnO NS hybrids, the characteristic peaks of the hexagonal wurtzite ZnO phase (JCPDS No. #36-1451) can be seen. Compared with the XRD results of ZnO NS, the peaks of $Ti_3C_2T_x$–ZnO NS at 31.3°, 33.9°, 35.7°, 47.2°, 56.3° and 62.6° can be indexed as the (100), (002), (101), (102), (110) and (103) planes, respectively. The 2θ of $Ti_3C_2T_x$–ZnO NS were shifted by a certain offset to a

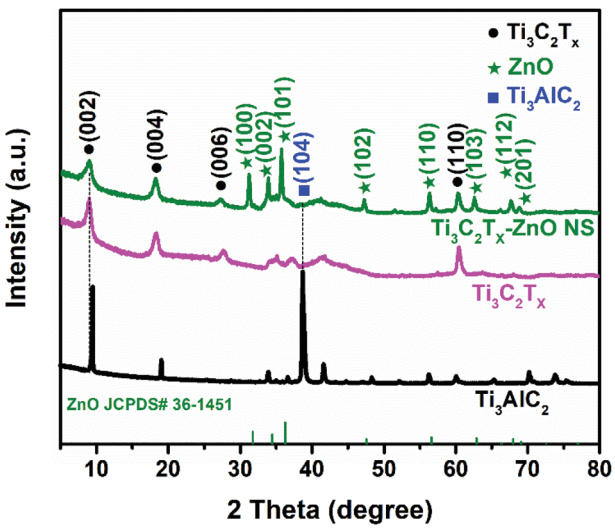

Fig. 3 XRD patterns for Ti_3AlC_2, $Ti_3C_2T_x$ and $Ti_3C_2T_x$–ZnO NS, respectively.

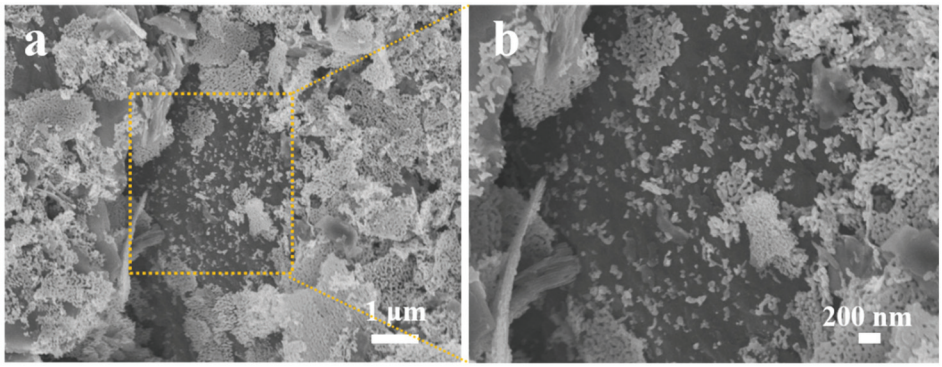

Fig. 4 $Ti_3C_2T_x$–ZnO nanosheet hybrids. (a) SEM image of $Ti_3C_2T_x$–ZnO nanosheet hybrids, (b) enlarged area in (a).

small angle, which is because of the bonding effect of $Ti_3C_2T_x$ and ZnO NS.

Fig. 4 shows the SEM images of $Ti_3C_2T_x$–ZnO NS, and it is noticeable that the $Ti_3C_2T_x$ and ZnO nanosheets were well hybridized. ZnO NS covered on the surface of the $Ti_3C_2T_x$ nanosheets. Due to the ZnO NS being composed of nanoparticles, they are destroyed and decomposed into nanoparticles after violent ultrasonication. Numerous ZnO nanoparticles were distributed on the $Ti_3C_2T_x$ sheet, which can provide more active sites and promote improvement in the gas-sensing performance. As shown in Fig. S6a and b,† Ti_3AlC_2 (MAX) displayed a layer-by-layer morphology. The $Ti_3C_2T_x$ (MXene) nanosheets presented obvious accordion-like morphology after the etching treatment with HF solution, and the spacing between the layers increased significantly. The morphology of the ZnO NS is shown in Fig. S6c and d.† It is worth noting that there are many gaps between the particles of the ZnO nanosheets, which will boost the gas transmission and adsorption in the $Ti_3C_2T_x$–ZnO NS materials.

To further confirm the structure and element composition of $Ti_3C_2T_x$ and $Ti_3C_2T_x$–ZnO NS, TEM and EDX mapping were carried out, as shown in Fig. 5. Fig. 5a shows the TEM image of $Ti_3C_2T_x$, which presented a clear layer structure. The high-resolution TEM (HRTEM) image of $Ti_3C_2T_x$ is shown in Fig. 5b. The lattice fringes with a spacing of 0.7 nm can be indexed with (002) of $Ti_3C_2T_x$. The TEM and HRTEM images of $Ti_3C_2T_x$–ZnO NS are shown in Fig. 5c and d. The ZnO NS are distributed on the surface of the $Ti_3C_2T_x$ nanosheets. Lattice fringes with different spacings of 0.25 nm and 0.248 nm correspond to (006) of $Ti_3C_2T_x$ and (101) of ZnO, respectively. The STEM, EDX mapping images (Fig. 5e) and EDX analysis (Fig. S7b†) demonstrate the uniform distribution of Ti, C, Zn, O and F elements on the $Ti_3C_2T_x$–ZnO NS, which indicates the close connection between the $Ti_3C_2T_x$ and ZnO NS. The selective area electron diffraction illustrated in Fig. S7a† indicates that the $Ti_3C_2T_x$–ZnO NS hybrid material is a composite phase and that these two materials have been successfully hybridized with each other.

The chemical bond composition and surface electronic valence of $Ti_3C_2T_x$, ZnO nanosheets and $Ti_3C_2T_x$–ZnO NS were

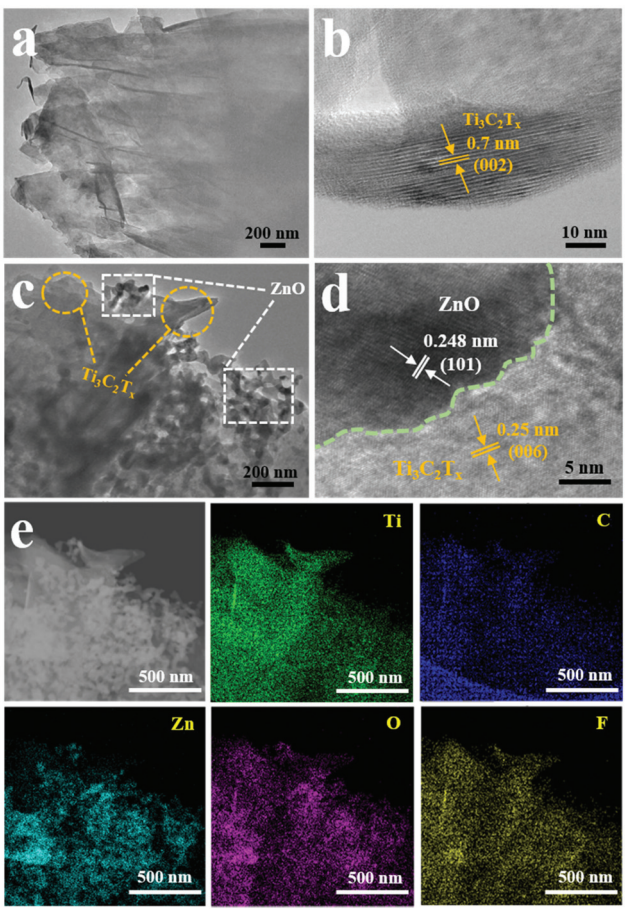

Fig. 5 (a) TEM and (b) HRTEM images of $Ti_3C_2T_x$. (c) TEM and (d) HRTEM images of $Ti_3C_2T_x$–ZnO NS. (e) The STEM image of $Ti_3C_2T_x$–ZnO NS and EDX mapping images of Ti, C, Zn, O and F elements.

measured by XPS analysis. The XPS full survey spectra illustrated the Ti, C, O and F elements in bare $Ti_3C_2T_x$ MXene, and the Zn and O elements that existed in the ZnO NS (Fig. 6a). The elements of Ti, C, Zn, O and F were found in the $Ti_3C_2T_x$–ZnO NS, and the intensity of the peaks assigned to Ti 2p and C 1s decreased on formation of the $Ti_3C_2T_x$ hybrids with ZnO

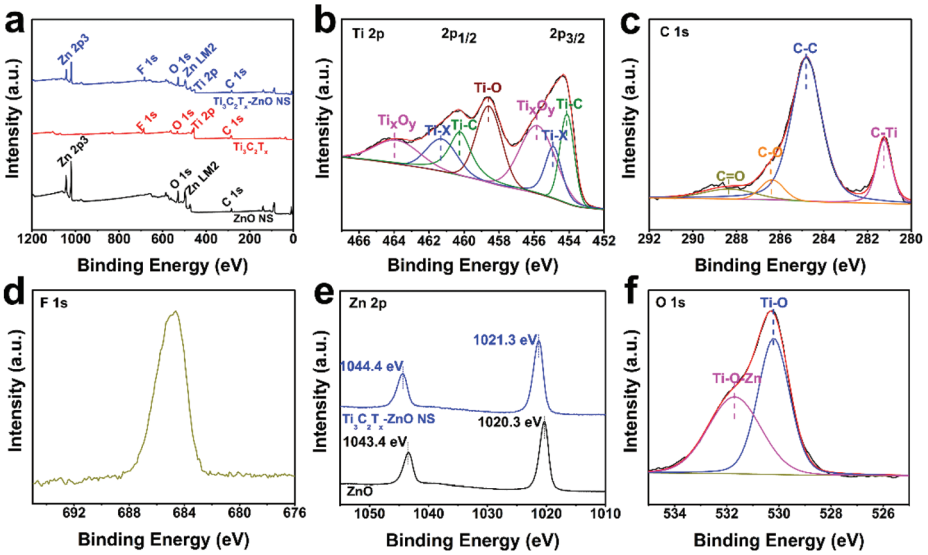

Fig. 6 (a) Full survey XPS spectrum of $Ti_3C_2T_x$, ZnO nanosheets and $Ti_3C_2T_x$–ZnO nanosheet hybrids. High-resolution XPS spectra for (b) Ti 2p, (c) C 1s, (d) F 1s, (e) Zn 2p and (f) O 1s of $Ti_3C_2T_x$–ZnO nanosheet hybrids.

NS. The Ti 2p of $Ti_3C_2T_x$ showed three bonds, including Ti–C, Ti–X and TiO_2.[64,65] The peaks with binding energy positioned at 455.1 eV can be ascribed to Ti–C, and the peaks located at 455.9 eV and 461.3 eV can be attributed to Ti-X. Other peaks at 457.1 eV and 461.8 eV correspond to TiO_2 (Ti^{4+}) (Fig. S8a†). As shown in Fig. 6b, the Ti 2p core-level spectrum can be splinted into Ti $2p_{1/2}$ and Ti $2p_{3/2}$. The peaks at 454.1 eV and 460.2 eV correspond to the Ti–C bond and other peaks at 454.9 eV and 461.3 eV can be ascribed to the Ti–X bond. The peaks at 458.6 eV can be assigned to the Ti–O bond. Other peaks at 455.8 eV and 463.8 eV can be assigned to Ti_xO_y (Ti^{3+}).[33,66] The C 1s core level of $Ti_3C_2T_x$ displayed in Fig. S8b† can be splinted into C–Ti, C–Ti–O, C–C and C–O peaks, which are located at 281.1 eV, 282.2 eV, 284.8 eV and 284.9 eV, respectively.[23,67] The C 1s core level of $Ti_3C_2T_x$–ZnO NS can be deconvoluted into four chemical bonds, as illustrated in Fig. 6c. The binding energies of 281.2 eV, 282.2 eV, 284.8 eV and 284.9 eV were attributed to C–Ti, C–C, C–O and C═O, respectively.[35] Meanwhile, the intensity and spacing of peaks corresponding to F 1s decreased in the $Ti_3C_2T_x$–ZnO NS compared with the pure $Ti_3C_2T_x$ sheet (Fig. 6a, d and Fig. S8c†). The peaks located at 1020.3 eV and 1043.4 eV were assigned to Zn $2p_{3/2}$ and Zn $2p_{1/2}$ of pure ZnO NS, respectively. In comparison, the binding energy of the Zn $2p_{3/2}$ and Zn $2p_{1/2}$ peaks in $Ti_3C_2T_x$–ZnO NS both shifted 1 eV and were located at 1021.3 eV and 1044.4 eV, respectively (Fig. 6e).[38] The O 1s core level of ZnO NS presented in Fig. S8d† can be splinted into O_L (lattice oxygen), O_V (vacancy oxygen) and O_A (adsorbed oxygen) located at 529.8 eV, 530.9 eV and 532.9 eV, respectively.[68] The vacancy oxygen occupies the majority of the O 1s, which indicates that abundant oxygen vacancies exist in the surface of ZnO. In contrast, the O 1s core level of $Ti_3C_2T_x$–ZnO NS displayed in Fig. 6f can be deconvoluted into Ti–O and Ti–O–Zn, located at 530.2 eV and 531.7 eV, respectively.[69]

Gas-sensing tests were conducted to explore the sensing performance of $Ti_3C_2T_x$, ZnO NS and $Ti_3C_2T_x$–ZnO NS gas sensors. Fig. 7a shows the dynamic response and recovery curves of pure $Ti_3C_2T_x$ and $Ti_3C_2T_x$–ZnO NS sensors to 20 ppm NO_2 under UV light at room temperature. The resistance of the $Ti_3C_2T_x$–ZnO NS sensor displayed a rapid increase from 511.8 MΩ to 2395.1 MΩ within a fast response speed (22 s) after exposure to NO_2. Meanwhile, the $Ti_3C_2T_x$–ZnO NS sensor exhibited a higher response (367.63% to 20 ppm NO_2) compared with the $Ti_3C_2T_x$ sensor (10.18% to 20 ppm NO_2) in a similar response time. After the resistance remains at a stable value, both gas sensors are unable to recover to the original resistance value. When 365 nm UV illumination was applied to assist the recovery process, the $Ti_3C_2T_x$–ZnO NS sensor showed an obvious change of resistance and a fast recovery speed (10 s), whereas the $Ti_3C_2T_x$ sensor still had no change. The NO_2 sensing performance of ZnO NS was also examined and is shown in Fig. S9.† The ZnO NS exhibited a large resistance and vibration at room temperature. In addition, the ZnO NS sensor had no significant response after contact with 20 ppm NO_2 gas. Fig. 7b illustrates the five cycle tests for the $Ti_3C_2T_x$–ZnO NS sensor to 20 ppm NO_2 at room temperature and recovery under UV illumination, demonstrating an excellent reproducibility without major changes.

The selectivity of the $Ti_3C_2T_x$–ZnO NS sensor to various gases was investigated, including 20 ppm NO_2 and 50 ppm of NH_3, CO_2, H_2 and hexanal, as shown in Fig. 7c. The responses to NO_2, NH_3, CO_2, H_2 and hexanal were 367.63%, 7.27%, 58.23%, 0% and 4.66%, respectively. The sensor exhibited a high selectivity towards NO_2 gas over the other gases. As shown in Fig. 7d, the $Ti_3C_2T_x$–ZnO NS sensor was exposed to different concentrations of NO_2 gas at room temp-

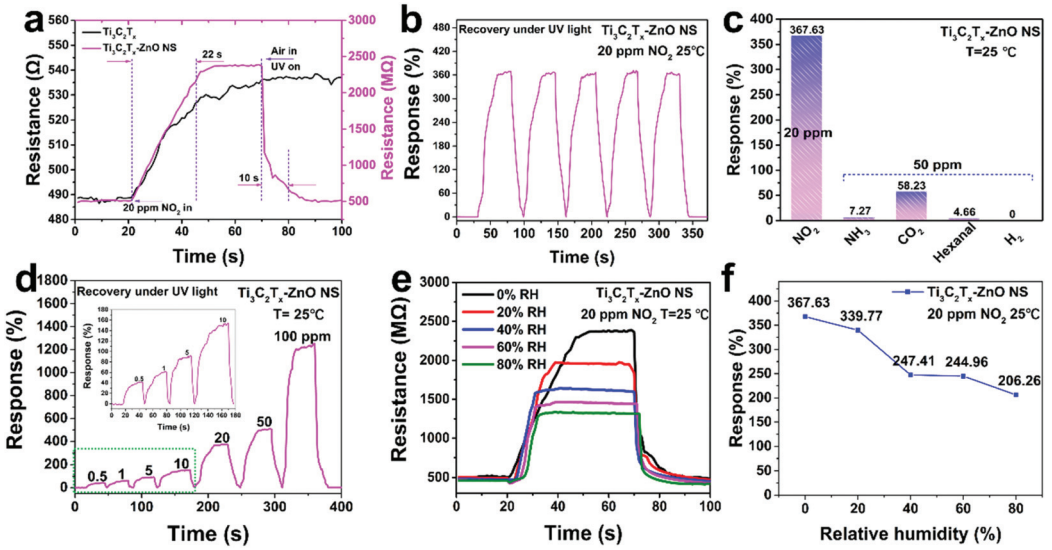

Fig. 7 (a) Dynamic response and recovery curves under UV irradiation for $Ti_3C_2T_x$ MXene and $Ti_3C_2T_x$–ZnO NS sensors to 20 ppm NO_2 at room temperature. (b) Repeatability tests of $Ti_3C_2T_x$–ZnO NS sensor to 20 ppm NO_2 at room temperature. (c) Selectivity of $Ti_3C_2T_x$–ZnO NS sensor to 20 ppm NO_2 and various target gases with a concentration of 50 ppm at room temperature. (d) Dynamic response and recovery curves of $Ti_3C_2T_x$–ZnO NS sensor under UV illumination to 0.5–100 ppm NO_2 at room temperature. (e) Dynamic response and recovery tests for the $Ti_3C_2T_x$–ZnO NS sensor in the RH ranging from 0% to 80% RH. (f) The response values of the $Ti_3C_2T_x$–ZnO NS sensor at different humidity conditions ranging from 0% to 80% RH.

erature and recovery under UV illumination. The responses of the sensor were increased with the concentration of NO_2 gas varying from low concentration to high concentration. Fig. 7e and f shows the responses of the $Ti_3C_2T_x$–ZnO NS sensor to 20 ppm NO_2 gas at room temperature under different RH conditions. The responses of the sensor decreased with increase in RH, with the responses being 367.63% (0% RH), 339.77% (20% RH), 247.41% (40% RH), 244.96% (60% RH) and 206.26% (80% RH), separately. With RH increasing from 0% to 80%, the response of the $Ti_3C_2T_x$–ZnO NS sensor to NO_2 gas exhibits a decrease, which is mainly because the water molecules covered the active sites and hindered the gas molecules adsorbed onto the surface of the material. More importantly, the sensor can remain at a relatively high response whether in a low-humidity or high-humidity environment, suggesting great potential in further applications. In addition, the long-term gas-sensing performance of the $Ti_3C_2T_x$–ZnO NS sensor was determined and is displayed in Fig. S10.† Significantly, the gas sensor exhibited a relatively high response (>275% to 20 ppm NO_2) after four weeks, indicating that the gas sensor can be used for a long time. To investigate the structural stability of $Ti_3C_2T_x$–ZnO NS, Raman analysis was carried out and the spectra are displayed in Fig. S11.† Raman peaks located at 156 cm^{-1} and 207 cm^{-1} correspond to the A_{1g} vibration modes of $Ti_3C_2T_x$.[32] Meanwhile, the small Raman peaks located at 434 cm^{-1} correspond to the E_2 (high) vibration mode of ZnO in the wurtzite structure.[13] It is notable that after 30 minutes of UV illumination the corresponding Raman peaks show almost no change. The results indicate that the $Ti_3C_2T_x$–ZnO NS can retain its structure without any destruction after a long period of UV illumination (365 nm, 3 mW cm^{-2}). Fig. S13† illustrates the response of $Ti_3C_2T_x$–ZnO NS towards 365 nm UV light (3 mW cm^{-2}) without NO_2 gas at room temperature. The $Ti_3C_2T_x$–ZnO NS exhibited periodic and stable resistance changes under UV light. In terms of the response process of $Ti_3C_2T_x$–ZnO NS towards NO_2 gas, the resistance of $Ti_3C_2T_x$–ZnO NS was increased when exposed to NO_2 gas. Therefore, the UV light illumination cannot provide enhancement to the sensor response, but only acts in the role of assisting the recovery of the sensor after the desorption of NO_2 gas. The UV light-induced gas desorption could help to accelerate the recovery process of the $Ti_3C_2T_x$–ZnO NS gas sensor.[70] In addition, comparison of the NO_2 sensing performances of the various gas sensors under UV illumination, including response/recovery time and sensitivity, are illustrated in Table S1.† The $Ti_3C_2T_x$–ZnO NS sensor exhibited better response and recovery properties compared with other reported NO_2 sensors. It is important that the $Ti_3C_2T_x$–ZnO NS sensor only needs a short period of external UV light illumination (10 s) in the recovery stage to achieve full recovery, while other reported NO_2 sensors can only be fully recovered after being exposed to UV light for a long time during the entire stage.

DFT calculations were carried out to explore the sensing properties of $Ti_3C_2T_x$ and ZnO to NO_2 gas. The flat model was constructed by a monolayer MXene and ZnO with a supercell of size of 3 × 3 × 1. The supercell of MXene ($Ti_3C_2T_x$) and ZnO was relaxed until the energy and the Hellmann–Feynman force reached the convergence criteria of 10^{-6} eV and 0.01 eV $Å^{-1}$. The optimized structures of NO_2 absorbed on $Ti_3C_2T_x$ and ZnO are illustrated in Fig. 8a and b. The adsorption energies of

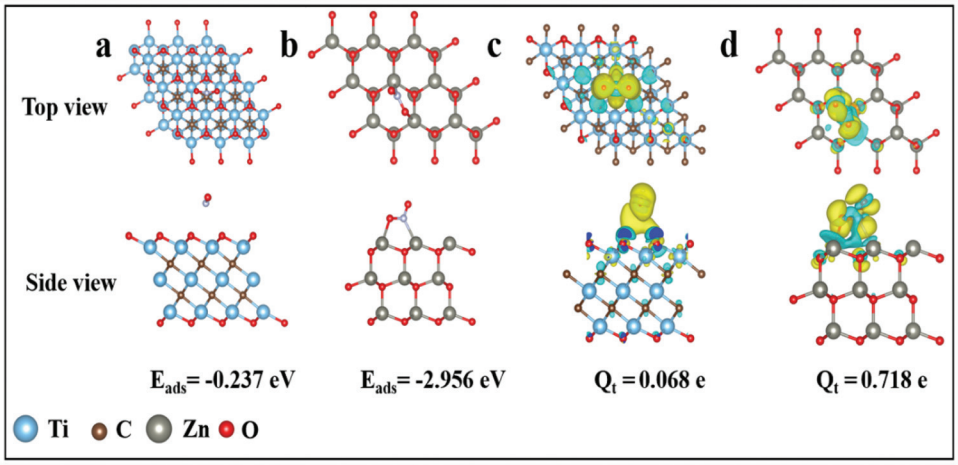

Fig. 8 Top and side view of the most energetically favorable configuration (a) $Ti_3C_2T_x$ and (b) ZnO after adsorption of NO_2 and the difference charge density plots of NO_2 adsorbed on the (c) $Ti_3C_2T_x$ and (d) ZnO using an isovalue of 0.0001 e $Å^{-3}$ and 0.002 e $Å^{-3}$, respectively. Cyan: charge depletion. Yellow: charge accumulation.

$Ti_3C_2T_x$ and ZnO for the NO_2 molecule were calculated using the following equation:

$$E_{ads} = E_{total} - E_{gas\ molecule} - E_{substrate} \quad (1)$$

where E_{total}, $E_{gas\ molecule}$ and $E_{substrate}$ represent the total energy of the substrate with gas molecule adsorbed, the gas molecule (which is NO_2 here) and the substrate, respectively. The adsorption energies of NO_2 on $Ti_3C_2T_x$ and ZnO were −0.237 eV and −2.956 eV, respectively. The results revealed that NO_2 gas was more easily adsorbed onto the ZnO, which has a higher adsorption energy towards NO_2 molecule than does $Ti_3C_2T_x$. Meanwhile, the charge transfer (Q_t) of the optimized configuration was 0.068e and 0.718e, respectively, for NO_2 for $Ti_3C_2T_x$ and ZnO, with the charge difference density unveiled in Fig. 8c and d. The results demonstrate that the interaction between the NO_2 molecule and ZnO is stronger than that with $Ti_3C_2T_x$. Furthermore, the results indicate that NO_2 mainly extracted electrons from ZnO, and the amount of electrons gained by NO_2 from $Ti_3C_2T_x$ can be neglected. Additionally, the O atom and N atom of NO_2 have formed a chemical bond with the Zn atom of ZnO, which means there is a chemical adsorption interaction. The bond lengths of Zn–O and Zn–N were calculated as 2.125 Å and 2.173 Å, respectively. The equilibrium heights of the N atom from the surface of $Ti_3C_2T_x$ and ZnO were 2.536 Å and 1.88 Å, respectively, as displayed in Table S2.†

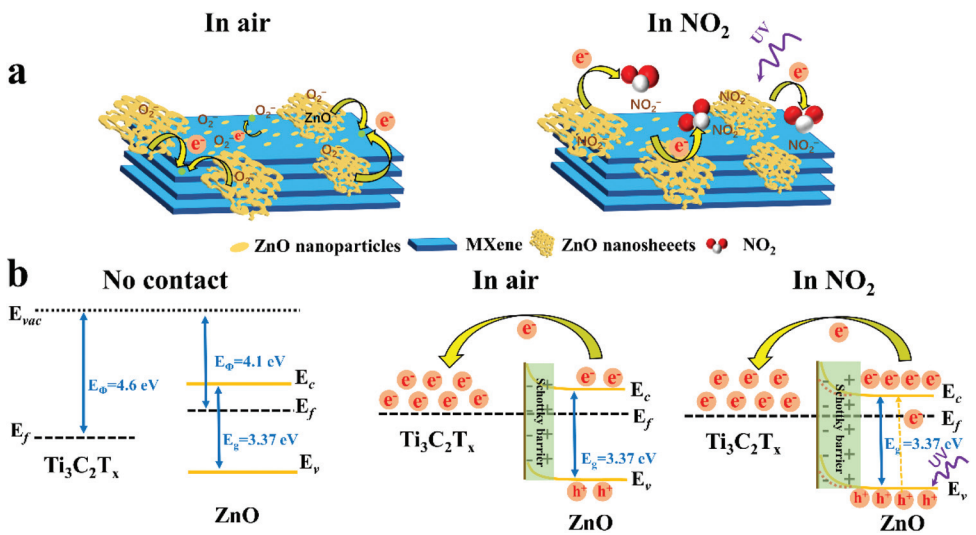

Fig. 9 (a) Schematic diagram of the possible gas-sensing mechanism of $Ti_3C_2T_x$–ZnO NS. (b) Energy band structure diagram of $Ti_3C_2T_x$–ZnO NS Schottky barriers in air and NO_2.

BET analysis was carried out to explore the specific area of samples, as displayed in Fig. S12.† Compared with pure $Ti_3C_2T_x$, the $Ti_3C_2T_x$–ZnO NS exhibits a higher BET specific surface area (9.71 m^2 g^{-1}) than $Ti_3C_2T_x$ (1.47 m^2 g^{-1}). The results illustrate that more active sites exist in the $Ti_3C_2T_x$–ZnO NS, which could provide the high sensitivity of $Ti_3C_2T_x$–ZnO NS toward NO_2 gas. The gas-sensing mechanism of the $Ti_3C_2T_x$–ZnO NS sensor can be explained by the charge transfer process. Fig. 9a shows the adsorption process when $Ti_3C_2T_x$–ZnO NS is exposed to air. Oxygen molecules are adsorbed onto the surface of ZnO NS and $Ti_3C_2T_x$ nanosheets, capturing the electrons from the conduction band of the materials and forming the chemisorbed oxygen species (O_2^-).[71,72] The specific reaction process is shown in the equations below:

$$O_2\ (\text{gas}) \rightarrow O_2\ (\text{ads}) \quad (2)$$

$$O_2\ (\text{ads}) + e^- \rightarrow O_2^-(\text{ads}) \quad (3)$$

Since the work function of $Ti_3C_2T_x$ (4.60 eV)[32] is higher than that of ZnO (4.1 eV),[73] the electrons of ZnO flow to $Ti_3C_2T_x$ until the Femi energy level reaches equilibrium. Consequently, the Schottky barrier layer is formed at the interface between $Ti_3C_2T_x$ and ZnO after the electron transfer process, as shown in Fig. 9b. Because the electron affinity of NO_2 (2.30 eV) is higher than O_2 (0.44 eV),[8] electrons will move towards NO_2 and yield NO_2^- ions, as illustrated in eqn (4). The electrons are continuously captured from ZnO nanosheets and flow to the $Ti_3C_2T_x$, resulting in enlargement of the Schottky barrier layer at the interface between $Ti_3C_2T_x$ and ZnO. Meanwhile, as a result of ZnO becoming less doped as electrons are captured by NO_2, and large amounts of electron transfer from ZnO to $Ti_3C_2T_x$, the Schottky barrier widens at the same time. In addition, the XPS results in Fig. 6e and f provide some important information. In Fig. 6e, the Zn 2p peaks of $Ti_3C_2T_x$–ZnO are shifted 1 eV towards higher binding energy compared with the Zn 2p peaks of pure ZnO, which can provide an evidence of the transfer of electrons from ZnO to $Ti_3C_2T_x$. In Fig. 6f, the formation of Ti–O–Zn chemical bonds indicates the strong interaction between $Ti_3C_2T_x$ and ZnO. The Ti–O–Zn chemical bonds that exist in the $Ti_3C_2T_x$–ZnO NS can effectively enhance the transfer efficiency of the barriers between these two materials.[6]

$$NO_2\ (\text{gas}) + e^- \rightarrow NO_2^-(\text{ads}) \quad (4)$$

The enhanced sensing properties can be attributed to the formation of the Schottky barrier layer and the increase in active sites on the surface of $Ti_3C_2T_x$–ZnO NS. It can be seen from Fig. 4 that large amounts of ZnO nanoparticles are uniformly distributed on the surface of the $Ti_3C_2T_x$ nanosheets, which can increase the number of active sites. Apart from these, large surface groups, such as –F, –OH and –O, exist in the $Ti_3C_2T_x$ nanosheets.[74,75] Therefore, more gas molecules could easily adsorb onto the surface of $Ti_3C_2T_x$–ZnO NS. The above features of the $Ti_3C_2T_x$–ZnO NS all play a role in enhancing the gas-sensing performance. The short recovery time of $Ti_3C_2T_x$–ZnO NS is mainly ascribed to the increase in the concentration of photogenerated holes of ZnO when it is under UV illumination (365 nm). The reason is that NO_2^- could react with the photogenerated holes on the valence band of ZnO and convert into NO_2 gas. The specific response and recovery process of $Ti_3C_2T_x$–ZnO NS to NO_2 gas is shown in Fig. S14† and the reactions of the recovery process are illustrated in eqn (5) and (6).[76,77] Therefore, the recovery time will decrease significantly. The most important thing is that the light only assists the sensor to recover quickly, rather than the entire response/recovery process, which helps to maintain the stability of the sensor. Therefore, the sensor will not be affected by long-term light illumination, which leads to performance degradation. Nevertheless, NO_2 sensing properties can be enhanced through the surface groups (including –F, –O and –OH) on the $Ti_3C_2T_x$, and abundant oxygen vacancies act as active sites to adsorb large amounts of NO_2 molecules.

$$h\nu \rightarrow h^+\ (h\nu) + e^-(h\nu) \quad (5)$$

$$NO_2^-(\text{ads}) + h^+\ (h\nu) \rightarrow NO_2\ (\text{g}) \quad (6)$$

Conclusions

In summary, $Ti_3C_2T_x$–ZnO NS for NO_2 detection at room temperature has been prepared by a facile sonication method. The sensor exhibited a 367.63% response, and a short response time (22 s) to 20 ppm NO_2 gas at room temperature. Meanwhile, the recovery time was 10 s under 365 nm UV illumination. The sensor also displayed superior reproducibility for five cycles of response tests to 20 ppm NO_2. Humidity tests demonstrated excellent anti-humidity properties when the sensor was operated under different humidity conditions. The predominant factor for the gas-sensing performance can be attributed to the abundant active sites in $Ti_3C_2T_x$–ZnO NS and the large quantity of photogenerated barriers of ZnO nanosheets under UV illumination. In addition, UV illumination excites the electrons and holes of ZnO NS, which speeds up the desorption process. The construction of $Ti_3C_2T_x$–ZnO NS Schottky junctions not only improves the sensing performance, but also solves the problems of poor sensitivity under humid conditions and easy oxidation. DFT calculations showed that the adsorption energy between NO_2 molecules and ZnO was stronger than that with $Ti_3C_2T_x$. Moreover, the difference charge transfer density plot illustrated that the NO_2 gas mainly extracted electrons from ZnO, indicating the high response of ZnO toward the NO_2 gas. Therefore, the combination of the novel $Ti_3C_2T_x$ material (high conductivity) with conventional metal oxide material (strong absorbability), as well as utilizing the photosensitivity of ZnO to generate photogenerated carriers under UV illumination, can provide new ideas for the further improvement of $Ti_3C_2T_x$-based gas sensors.

Author contributions

Chao Fan: Conceptualization, methodology, investigation, formal analysis, visualization, data curation, writing original draft. Jia Shi: Formal analysis, writing-review and editing. Yongwei Zhang: Writing-review and editing. Wenjing Quan: Writing-review and editing. Xiyu Chen: Writing-review and editing. Jianhua Yang: Supervision, conceptualization, methodology, funding acquisition, writing-review and editing. Min Zeng: Resources, writing-review and editing. Zhihua Zhou: Writing-review and editing. Yanjie Su: Writing-review and editing. Hao Wei: Writing-review and editing. Zhi Yang: Resources, supervision, funding acquisition, writing-review and editing.

Conflicts of interest

There are no conflicts to declare.

Acknowledgements

This work was supported by the National Natural Science Foundation of China (62101329 and 61971284), Shanghai Sailing Program (21YF1421400), the Oceanic Interdisciplinary Program of Shanghai Jiao Tong University (SL2020ZD203, SL2020MS031, and SL2021MS006) and the Scientific Research Fund of Second Institute of Oceanography, Ministry of Natural Resources of P. R. China (SL2003), and Startup Fund for Youngman Research at Shanghai Jiao Tong University. We also acknowledge analysis support from the Instrumental Analysis Center of Shanghai Jiao Tong University and the Center for Advanced Electronic Materials and Devices of Shanghai Jiao Tong University.

References

1 Y. Kim, K. C. Kwon, S. Kang, C. Kim, T. H. Kim, S. P. Hong, S. Y. Park, J. M. Suh, M. J. Choi, S. Han and H. W. Jang, *ACS Sens.*, 2019, **4**, 2395–2402.
2 Z. Li, Y. Liu, D. Guo, J. Guo and Y. Su, *Sens. Actuators, B*, 2018, **271**, 306–310.
3 Y. Huang, W. Jiao, Z. Chu, G. Ding, M. Yan, X. Zhong and R. Wang, *J. Mater. Chem. C*, 2019, **7**, 8616–8625.
4 M. Urso, S. G. Leonardi, G. Neri, S. Petralia, S. Conoci, F. Priolo and S. Mirabella, *Sens. Actuators, B*, 2020, **305**, 127481.
5 H. Zhang, L. Yu, Q. Li, Y. Du and S. Ruan, *Sens. Actuators, B*, 2017, **241**, 109–115.
6 J. Hao, D. Zhang, Q. Sun, S. Zheng, J. Sun and Y. Wang, *Nanoscale*, 2018, **10**, 7210–7217.
7 V. B. Raj, A. T. Nimal, M. Tomar, M. U. Sharma and V. Gupta, *Sens. Actuators, B*, 2015, **220**, 154–161.
8 Z. Wang, G. Men, R. Zhang, F. Gu and D. Han, *Sens. Actuators, B*, 2018, **263**, 218–228.
9 K. Y. Ko, J. G. Song, Y. Kim, T. Choi, S. Shin, C. W. Lee, K. Lee, J. Koo, H. Lee, J. Kim, T. Lee, J. Park and H. Kim, *ACS Nano*, 2016, **10**, 9287–9296.
10 J. Pan, W. Liu, L. Quan, N. Han, S. Bai, R. Luo, Y. Feng, D. Li and A. Chen, *Ind. Eng. Chem. Res.*, 2018, **57**, 10086–10094.
11 R. Kumar, N. Goel and M. Kumar, *ACS Sens.*, 2017, **2**, 1744–1752.
12 A. V. Agrawal, N. Kumar and M. Kumar, *Nano-Micro Lett.*, 2021, **13**, 38.
13 A. D. Ugale, G. G. Umarji, S. H. Jung, N. G. Deshpande, W. Lee, H. K. Cho and J. B. Yoo, *Sens. Actuators, B*, 2020, **308**, 127690.
14 B. G. Ghule, N. M. Shinde, S. D. Raut, S. F. Shaikh, A. M. Al-Enizi, K. H. Kim and R. S. Mane, *J. Colloid Interface Sci.*, 2021, **589**, 401–410.
15 Y. H. Kim, J. S. Park, Y.-R. Choi, S. Y. Park, S. Y. Lee, W. Sohn, Y.-S. Shim, J.-H. Lee, C. R. Park, Y. S. Choi, B. H. Hong, J. H. Lee, W. H. Lee, D. Lee and H. W. Jang, *J. Mater. Chem. A*, 2017, **5**, 19116–19125.
16 Y. Han, Y. Liu, C. Su, S. Wang, H. Li, M. Zeng, N. Hu, Y. Su, Z. Zhou, H. Wei and Z. Yang, *Sens. Actuators, B*, 2019, **296**, 126666.
17 Y. Han, Y. Ma, Y. Liu, S. Xu, X. Chen, M. Zeng, N. Hu, Y. Su, Z. Zhou and Z. Yang, *Appl. Surf. Sci.*, 2019, **493**, 613–619.
18 J. Guo, R. Wen, J. Zhai and Z. L. Wang, *Sci. Bull.*, 2019, **64**, 128–135.
19 F. Urban, F. Giubileo, A. Grillo, L. Iemmo, G. Luongo, M. Passacantando, T. Foller, L. Madauß, E. Pollmann, M. P. Geller, D. Oing, M. Schleberger and A. D. Bartolomeo, *2D Mater.*, 2019, **6**, 045049.
20 Y. Liu, Y. Wang, M. Ikram, H. Lv, J. Chang, Z. Li, L. Ma, A. U. Rehman, G. Lu, J. Chen and K. Shi, *ACS Sens.*, 2018, **3**, 1576–1583.
21 M. Donarelli, L. Ottaviano, L. Giancaterini, G. Fioravanti, F. Perrozzi and C. Cantalini, *2D Mater.*, 2016, **3**, 025002.
22 Y. Wang, J. Xue, X. Zhang, J. Si, Y. Liu, L. Ma, M. Ullah, M. Ikram, L. Li and K. Shi, *Mater. Sci. Semicond. Process.*, 2020, **110**, 104961.
23 S. Liu, M. Wang, G. Liu, N. Wan, C. Ge, S. Hussain, H. Meng, M. Wang and G. Qiao, *Appl. Surf. Sci.*, 2021, **567**, 150747.
24 Z. Zhu, C. Liu, F. Jiang, J. Liu, X. Ma, P. Liu, J. Xu, L. Wang and R. Huang, *J. Hazard. Mater.*, 2020, **399**, 123054.
25 C. Tan, X. Cao, X. Wu, Q. He, J. Yang, X. Zhang, J. Chen, W. Zhao, S. Han, G. H. Nam, M. Sindoro and H. Zhang, *Chem. Rev.*, 2017, **117**, 6225–6331.
26 K. S. Novoselov, A. Mishchenko, A. Carvalho and A. H. C. Neto, *Science*, 2016, **353**, aac9439.
27 P. K. Kannan, D. J. Late, H. Morgan and C. S. Rout, *Nanoscale*, 2015, **7**, 13293–13312.
28 F. Bu, M. M. Zagho, Y. Ibrahim, B. Ma, A. Elzatahry and D. Zhao, *Nano Today*, 2020, **30**, 100803.
29 D. Zhao, Z. Chen, W. Yang, S. Liu, X. Zhang, Y. Yu, W. C. Cheong, L. Zheng, F. Ren, G. Ying, X. Cao, D. Wang,

Q. Peng, G. Wang and C. Chen, *J. Am. Chem. Soc.*, 2019, **141**, 4086–4093.
30 C. Zhang, L. McKeon, M. P. Kremer, S. H. Park, O. Ronan, A. Seral-Ascaso, S. Barwich, C. Ó. Coileáin, N. McEvoy, H. C. Nerl, B. Anasori, J. N. Coleman, Y. Gogotsi and V. Nicolosi, *Nat. Commun.*, 2019, **10**, 1795.
31 B. Liu, L. Chen, G. Liu, A. N. Abbas, M. Fathi and C. Zhou, *ACS Nano*, 2014, **8**, 5304–5314.
32 J. Choi, Y. J. Kim, S. Y. Cho, K. Park, H. Kang, S. J. Kim and H.-T. Jung, *Adv. Funct. Mater.*, 2020, **30**, 2003998.
33 B. Sun, H. Lv, Z. Liu, J. Wang, X. Bai, Y. Zhang, J. Chen, K. Kan and K. Shi, *J. Mater. Chem. A*, 2021, **9**, 6335–6344.
34 T. Chen, W. Yan, Y. Wang, J. Li, H. Hu and D. Ho, *J. Mater. Chem. C*, 2021, **9**, 7407–7416.
35 C. Fan, F. Sun, X. Wang, Z. Huang, M. Keshvardoostchokami, P. Kumar and B. Liu, *Nanomaterials*, 2019, **9**, 1277.
36 H. Wang, M. Dai, Y. Li, J. Bai, Y. Liu, Y. Li, C. Wang, F. Liu and G. Lu, *Sens. Actuators, B*, 2021, **329**, 129145.
37 X. Yang, S. Zhang, Q. Yu, L. Zhao, P. Sun, T. Wang, F. Liu, X. Yan, Y. Gao, X. Liang, S. Zhang and G. Lu, *Sens. Actuators, B*, 2019, **281**, 415–423.
38 S. Zhao, Y. Shen, P. Zhou, F. Hao, X. Xu, S. Gao, D. Wei, Y. Ao and Y. Shen, *Sens. Actuators, B*, 2020, **308**, 127729.
39 L. Zhu and W. Zeng, *Sens. Actuators, A*, 2017, **267**, 242–261.
40 M. T. Vijjapu, S. G. Surya, S. Yuvaraja, X. Zhang, H. N. Alshareef and K. N. Salama, *ACS Sens.*, 2020, **5**, 984–993.
41 J. Wang, S. Fan, Y. Xia, C. Yang and S. Komarneni, *J. Hazard. Mater.*, 2020, **381**, 120919.
42 D.-B. Moon, A. Bag, H.-B. Lee, M. Meeseepong, D.-H. Lee and N.-E. Lee, *Sens. Actuators, B*, 2021, **345**, 130373.
43 P. T. Hung, P. D. Hoat, V. X. Hien, H. Y. Lee, S. Lee, J. H. Lee, J. J. Kim and Y. W. Heo, *ACS Appl. Mater. Interfaces*, 2020, **12**, 34274–34282.
44 Y. Song, F. Chen, Y. Zhang, S. Zhang, F. Liu, P. Sun, X. Yan and G. Lu, *Sens. Actuators, B*, 2019, **287**, 191–198.
45 Z. Li, S. Yan, S. Zhang, J. Wang, W. Shen, Z. Wang and Y. Q. Fu, *J. Alloys Compd.*, 2019, **770**, 721–731.
46 S. Zhang, L. Zhao, B. Huang and X. Li, *Sens. Actuators, B*, 2020, **319**, 128264.
47 M. Wang, Y. Zhu, Q. Luo, C. Ge, G. Liu, G. Qiao and E. J. Kim, *Appl. Surf. Sci.*, 2021, **566**, 150750.
48 W. Zheng, C. Yang, Z. Li, J. Xie, C. Lou, G. Lei, X. Liu and J. Zhang, *Sens. Actuators, B*, 2021, **329**, 129127.
49 Y. Zhou, C. Zou, X. Lin and Y. Guo, *Appl. Phys. Lett.*, 2018, **113**, 082103.
50 E. Wu, Y. Xie, B. Yuan, H. Zhang, X. Hu, J. Liu and D. Zhang, *ACS Sens.*, 2018, **3**, 1719–1726.
51 Y. Xia, L. Zhou, J. Yang, P. Du, L. Xu and J. Wang, *ACS Appl. Electron. Mater.*, 2020, **2**, 580–589.
52 J. Wang, Y. Shen, X. Li, Y. Xia and C. Yang, *Sens. Actuators, B*, 2019, **298**, 126858.
53 C. Feng, F. Wen, Z. Ying, L. Li, X. Zheng, P. Zheng and G. Wang, *Chem. Phys. Lett.*, 2020, **754**, 137745.
54 R. Bhardwaj and A. Hazra, *J. Mater. Chem. C*, 2021, **9**, 15735–15754.
55 K. Deshmukh, T. Kovářík and S. K. K. Pasha, *Coord. Chem. Rev.*, 2020, **424**, 213514.
56 M. Alhabeb, K. Maleski, B. Anasori, P. Lelyukh, L. Clark, S. Sin and Y. Gogotsi, *Chem. Mater.*, 2017, **29**, 7633–7644.
57 B. Hammer, L. B. Hansen and J. K. Nørskov, *Phys. Rev. B: Condens. Matter Mater. Phys.*, 1999, **59**, 7413–7421.
58 G. Kresse and J. Furthmüller, *Phys. Rev. B: Condens. Matter Mater. Phys.*, 1996, **54**, 11169–11186.
59 R. Stadler, W. Wolf, R. Podloucky, G. Kresse, J. Furthmüller and J. Hafner, *Phys. Rev. B: Condens. Matter Mater. Phys.*, 1996, **54**, 1729–1734.
60 S. Grimme, J. Antony, S. Ehrlich and H. Krieg, *J. Chem. Phys.*, 2010, **132**, 154104.
61 J. P. Perdew, W. Yang, K. Burke, Z. Yang, E. K. U. Gross, M. Scheffler, G. E. Scuseria, T. M. Henderson, I. Y. Zhang, A. Ruzsinszky, H. Peng, J. Sun, E. Trushin and A. Görling, *Proc. Natl. Acad. Sci. U. S. A.*, 2017, **114**, 2801–2806.
62 J. Shi, W. Quan, X. Chen, X. Chen, Y. Zhang, W. Lv, J. Yang, M. Zeng, H. Wei, N. Hu, Y. Su, Z. Zhou and Z. Yang, *Phys. Chem. Chem. Phys.*, 2021, **23**, 18359–18368.
63 G. Henkelman, A. Arnaldsson and H. Jónsson, *Comput. Mater. Sci.*, 2006, **36**, 354–360.
64 W. Yuan, K. Yang, H. Peng, F. Li and F. Yin, *J. Mater. Chem. A*, 2018, **6**, 18116–18124.
65 S. Sun, M. Wang, X. Chang, Y. Jiang, D. Zhang, D. Wang, Y. Zhang and Y. Lei, *Sens. Actuators, B*, 2020, **304**, 127274.
66 A. Hermawan, B. Zhang, A. Taufik, Y. Asakura, T. Hasegawa, J. Zhu, P. Shi and S. Yin, *ACS Appl. Nano Mater.*, 2020, **3**, 4755–4766.
67 M. Liu, Z. Wang, P. Song, Z. Yang and Q. Wang, *Ceram. Int.*, 2021, **47**, 23028–23037.
68 Q. Li, D. Chen, J. Miao, S. Lin, Z. Yu, D. Cui, Z. Yang and X. Chen, *Sens. Actuators, B*, 2021, **326**, 128952.
69 Y. Qian, H. Wei, J. Dong, Y. Du, X. Fang, W. Zheng, Y. Sun and Z. Jiang, *Ceram. Int.*, 2017, **43**, 10757–10762.
70 A. Grillo, E. Faella, A. Pelella, F. Giubileo, L. Ansari, F. Gity, P. K. Hurley, N. McEvoy and A. D. Bartolomeo, *Adv. Funct. Mater.*, 2021, **31**, 2105722.
71 M. Liu, Z. Wang, P. Song, Z. Yang and Q. Wang, *Sens. Actuators, B*, 2021, **340**, 129946.
72 Z. Yang, L. Jiang, J. Wang, F. Liu, J. He, A. Liu, S. Lv, R. You, X. Yan, P. Sun, C. Wang, Y. Duan and G. Lu, *Sens. Actuators, B*, 2021, **326**, 128828.
73 Y. Tong, T. Jiang, S. Qiu, K. Koshmak, A. Giglia, S. Kubsky, A. Bendounan, L. Chen, L. Pasquali, V. A. Esaulov and H. Hamoudi, *J. Phys. Chem. C*, 2018, **122**, 2880–2889.
74 Y. Li, Z. Yin, G. Ji, Z. Liang, Y. Xue, Y. Guo, J. Tian, X. Wang and H. Cui, *Appl. Catal., B*, 2019, **246**, 12–20.
75 J. Pang, R. G. Mendes, A. Bachmatiuk, L. Zhao, H. Q. Ta, T. Gemming, H. Liu, Z. Liu and M. H. Rummeli, *Chem. Soc. Rev.*, 2019, **48**, 72–133.
76 C. Han, X. Li, Y. Liu, X. Li, C. Shao, J. Ri, J. Ma and Y. Liu, *J. Hazard. Mater.*, 2021, **403**, 124093.
77 X. Chen, J. Hu, P. Chen, M. Yin, F. Meng and Y. Zhang, *Sens. Actuators, B*, 2021, **339**, 129902.